Electrochimica Acta 518 (2025) 145787

Contents lists available at ScienceDirect

Electrochimica Acta

journal homepage: www.journals.elsevier.com/electrochimica-acta

Optimization of a gold electrodeposited platform for the development of electrochemical immunosensors: The case of study of acute kidney injury

Francesca Polli [a,*], Rosaceleste Zumpano [a], Gianluca Zanellato [b], Sofia de Azeredo Pereira [c], Alessandro Fantoni [d,e], Franco Mazzei [a], M . Gabriela Almeida [f,g]

[a] Department of Chemistry and Drug Technologies, Sapienza University of Rome, P.le Aldo Moro 5, 00185,Rome, Italy
[b] Department of Basic and Applied Sciences for Engineering, Sapienza University of Rome, P.le Aldo Moro 5, 00185, Rome, Italy
[c] iNOVA4Health, NOVA Medical School|Faculdade de Ciências Médicas, NMS|FCM, Universidade NOVA de Lisboa (UNL), Portugal & Centro Clínico Académico de Lisboa (CCAL), Lisboa, Portugal
[d] Lisbon School of Engineering (ISEL)/IPL, Rua Conselheiro Emídio Navarro, n°1, 1959-007, Lisboa, Portugal
[e] CTS—Centre of Technology and Systems and Associated Lab of Intelligent Systems (LASI), 2829-516, Caparica, Portugal
[f] Egas Moniz Center for Interdisciplinary Research (CiiEM), Egas Moniz School of Health & Science, 2819-511, Caparica, Portugal
[g] Departamento de Química, Associate Laboratory i4HB – Institute for Health and Bioeconomy, UCIBIO – Applied Molecular Biosciences Unit, Faculdade de Ciências e Tecnologia, Universidade NOVA de Lisboa, 2829-516, Monte de Caparica, Portugal

ARTICLE INFO

Keywords:
SPCE
Electrodeposition
Immunosensor
NGAL
Acute kidney injury

ABSTRACT

In this work, we present a systematic approach for the optimization of a stable and reproducible platform for the development of unlabelled immunosensors based on electrodeposited (ED) gold nanoparticles (AuNPs) on screen-printed carbon electrodes (SPCEs). The modification was performed in a $[AuCl_4]^-$ solution sweeping the potential between 1.1 V and - 0.1 V vs Ag/AgClsat. The influence of the gold concentration and number of ED scans on surface morphology was investigated through Scanning Electron Microscopy (SEM), Energy dispersive X-ray (EDX), and Cyclic Voltammetry (CV). The results were discussed by considering the average AuNPs diameter determined for each modification and by comparing the features of the realized platforms to those of commercial gold screen-printed electrodes (SPEs). The best performing platform in terms of electrochemical behaviour, stability, and reproducibility was selected for the development of a label-free immunosensor. The target analyte was neutrophil-associated lipocalin (NGAL), a 25 kDa protein that serves as a biomarker for Acute Kidney Injury (AKI), one of the primary causes of in-hospital mortality globally. In contrast to creatinine, NGAL allows for the early prediction of AKI-related clinical events, facilitating timely interventions, which could significantly enhance outcomes in high-risk patients. To this aim, the electrode surface was first modified with a self-assembled monolayer (SAM) of 3-mercaptopropionic acid (MPA) and then functionalized by immobilizing the NGAL antibody via EDC/NHS coupling. The LOD (0.56 μg/mL) and the high sensitivity obtained (21.8 μA mL/μg) were compatible with the diagnostic range required for AKI.

1. Introduction

Gold-modified platforms have gained significant attention in electrochemical biosensors' research, due to several key factors including exceptional conductivity, electrocatalytic activity, high surface-to-volume ratio and versatility [1,2]. Moreover, the strong affinity of gold for thiols and other functional groups facilitates the formation of highly stable and biocompatible platforms allowing immobilization of biological molecules on the electrode surfaces [3,4]. These characteristics position make gold nanoparticles (AuNPs) among the most widely used nanomaterials for sensor fabrication. Consequently, as highlighted in recent review articles, AuNP-based biosensors have experienced exponential growth over the past two decades [1,5]. This trend was particularly prominent during the COVID-19 pandemic (2020–2022), where AuNPs emerged as a highly versatile and reliable platform for biosensing applications [6].

Throughout this time, another field that attracted much interest was that of immunosensors [7–9]. Thanks to specific advantages such as excellent electrical conductivity and a high surface area, immunosensors are highly sensitive devices capable of detecting extremely low

* Corresponding author at: Department of Chemistry and Drug Technologies, Sapienza University of Rome, P.le Aldo Moro 5, 00185, Rome, Italy.
E-mail address: francesca.polli@uniroma1.it (F. Polli).

https://doi.org/10.1016/j.electacta.2025.145787
Received 8 October 2024; Received in revised form 11 January 2025; Accepted 31 January 2025
Available online 1 February 2025

concentrations of analytes. Specifically the use of novel and different nanomaterials [10–13], bring to the nanosensors the advantage to investigate very small changes occurring at the sensor surface. Some examples can be found in recent works regarding labelled immunosensors, such as those developed on a nitrogen and boron-doped graphene quantum dots-platform specifically designed for the detection of cardiac troponin I (CTnI) [14] or the one fabricated by using of Ni/Cu-MOFs [15] for a tumor necrosis-factor-alpha (TNF-a) immunosensor. Furthermore, their chemical stability and rapid response times further enhance their suitability for point-of-care (POC) applications, eliminating the need for additional amplification, particularly in clinical settings where rapid screening can be crucial for reducing diagnosis time and enabling timely treatment. Moreover, aspects like affordability, portability, minimal sample volume, and low power consumption have greatly contributed to the widespread adoption of these devices for a wide range of other applications including environmental monitoring, agriculture and food industry which confirmes their versatility as valuable tools for real-time and on-site analysis.

However, unlike most electrochemical biosensors —where the signal typically arises from a redox centre within the biomolecule structure—native immunoglobulins lack electroactive sites. Thus, except in case of chemically labelled or conjugated antibodies, the electrochemical response of label-free immunosensors reflects the entire platform rather than that of the biomolecule itself [9,16,17]. In this context, the platform's stability and homogeneity play a crucial role; therefore, efforts have been made to enhance immunosensors' robustness, reproducibility, and sensitivity [1,9]. Nowadays, various approaches are employed to develop gold-based platforms, including the drop-casting of AuNPs [18] or the use of commercially available gold electrodes. However, commercially available electrodes [19] are rarely used in immunosensors development due to their high cost, and challenges such as poor reproducibility and proprietary manufacturing processes constraint. Furthermore, mass production of screen-printed electrodes (SPEs) for laboratories requires the need for high-temperature curing equipment and the gold ink impurities can affect sensor performance [19,20], also reducing the protein stability [21]. In contrast, nanoparticle drop-casting is among the most employed techniques, valued for its simplicity and ability to achieve efficient gold coverage [2]. However, several drawbacks have to be considered, including long synthesis times, instability, centrifugation steps, and reproducibility issues related to the formation of coffee-ring patterns onto the electrode surface [22]. To address these limitations, electrodeposition (ED) has emerged as a method for directly shaping gold on the electrode surface, ensuring a higher reproducibility and the ability to easily modify the surface morphology by adjusting the electrochemical parameters [23–25].

Nevertheless, while electrodeposition has been extensively studied for glassy carbon (GC) electrodes [23,26,27] through both theoretical and experimental approaches, less attention has been given to screen-printed carbon electrodes (SPCEs). Despite their widespread use as biosensor platforms due to their potential for miniaturization and versatility, comprehensive studies on the influence of scan numbers [28], gold concentration and supporting electrolytes [29] on morphology [30] in SPCEs are rarely outlined. Given the distinct features and reactivity of GC and SPCE, findings from GC cannot be directly applied to SPCE, which exhibits a different electrode morphology and reactivity [24,31].

Therefore, the present study aims to optimize the gold modification of SPCE surfaces and study its potential in immunosensing applications. To this aim, the impact of scan number and gold concentration was carefully evaluated using Scanning Electron Microscopy (SEM) and Cyclic Voltammetry (CV). Size-distribution curves were obtained for each of the five tested concentrations, and for the first time, how each surface evolves from 2 to 25 scan. Additionally, the morphology and Energy Dispersive X-ray (EDX) spectra were compared with those of a commercially available gold electrode.

To the best of our knowledge, this represents the most comprehensive study of electrodeposition on SPCEs available in the literature by cyclic voltammetry [32,33], and the first one optimized for immunosensing purposes. The optimized platform in terms of conductivity, reproducibility, and stability was then employed to build a label-free immunosensor for the Neutrophil Gelatinase-Associated Lipocalin (NGAL), a biomarker whose urinary levels are highly predictive of acute kidney injury (AKI) [34–38]. In fact, conventional diagnostic methods (i.e. serum creatinine and urine output), allows to identify AKI only after significant kidney damage has already taken place, while the NGAL protein is produced in response to kidney injury, reaches detectable levels in blood and urine within hours of the damage, much earlier than those of conventional biomarkers. Presently, NGAL detection is achieved through various methods [34]. Recently, the DNAse I-based sensor was developed, featuring a linear range from 12.5 to 400 pg/mL and a sensitivity of approximately 6.25 pg/mL [39], which is far below the NGAL cut-off (> 0.10 μg/mL) [34,37,40]. These types of sensors employ a specific enzyme immobilized on a polydopamine nanosphere/aptamer nanocomplex. However, their application is constrained by the need for specific reaction temperatures. In contrast, while immunosensors are generally less sensitive, they are not limited by temperature requirements. Neves et al. [41] for instance, reported a sanwhich labelled-immunosensor with a limit of detection (LOD) of 96 pg/mL. Nevertheless, a narrow linear range of 0.15 to 2 ng/mL restricts its applicability. Moreover, like most labelled immunoassays, requires longer measurement times (around 125 mins) due to the additional steps involved after NGAL binding. On the other hand, in Yukird's study [42], the antibody was immobilized on a graphene/polyaniline nanocomposite, achieving a LOD of 21.1 ng/mL and a linear range between 50 and 500 ng/mL. The quantity of antibody required for this immunoassay is, however, unusually high, limiting its application. A greater sensitivity was achieved in the works of Phonklam [43] and Wang [44], which maintained excellent performance using fabrication procedures based on gold sputtering atop polypropylene and PET electrodes, respectively. Despite the excellent analytical performance, compatible with the determination of NGAL for AKI, the preparation of these electrodes requires additional equipment beyond that used for measurements. In this context, electrodeposition proves to be a valuable tool for obtaining a versatile platform on commercial electrodes in a reproducible manner, avoiding the use of specific reagents and allowing customization of both the procedure and the electrode surface by simply adjusting the applied electrochemical parameters. Given the high catalytic activity of gold particles, the first part of this study was dedicated to developing a stable electrodeposition platform with high reproducibility [45]. Subsequently, the surface was modified using a thiolic compound with carboxylic moieties, which were activated through N-(3-Dimethylaminopropyl)-N'-ethylcarbodiimide (EDC)/N—Hydroxysuccinimide (NHS) chemistry to perform antibody (Ab) immobilization. Once the surface was properly deactivated, the sensor was calibrated using NGAL standards solutions. The minimal interference and the good agreement with spiked urine samples demonstrate its potential use for the AKI prediction.

2. Materials and methods

2.1. Materials

Sulfuric acid (H_2SO_4), Chloroauric acid colloidal gold solution ($HAuCl_4$), 3-(N-morpholino)propanesulfonic acid (MES), potassium chloride (KCl), 3-mercaptopropionic acid (3-MPA), urea, glutamic acid, ascorbic acid, glycine, sodium phosphate monobasic (NaH_2PO_4), bovine serum albumin (BSA), sodium phosphate dibasic (Na_2HPO_4), potassium chloride (KCl), potassium ferricyanide trihydrate ($K_3[Fe(CN)_6]\cdot 3H_2O$), potassium ferrocyanide hexahydrate ($K_4[Fe(CN)_6]\cdot 6H_2O$), 2-(N-morpholino)ethanesulfonic acid (MES), *N*-hydroxisuccinimide (NHS), N-(3-Dimethylaminopropyl)-N′-ethylcarbodiimide hydrochloride (EDC) and 3-mercaptopropionic acid (3-MPA) were obtained from Sigma Aldrich

(St. Louis, MO, USA). NGAL Monoclonal Antibody and NGAL protein antibody were purchased from Abcam (Cambridge, UK) and were stored at −20 °C in aliquots of respectively 10 μg/mL and 100 μg /mL in 10 mM PBS buffer pH 7.4 to avoid repeated freeze and thaw cycles. All solutions were prepared using Milli-Q water (18.2 MΩ·cm, at 25 °C; TOC < 10 μg L^{-1}, Millipore, Bedford, MA, USA).

2.2. Electrochemical and surface characterization apparatus

The ED process was set up in a three-electrode electrochemical cell by employing an SPCE electrode (d = 4 mm, A = 0.126 mm^2) as a working electrode (WE), a graphite lead as a counter electrode (CE) and $Ag/AgCl_{sat}$ as a reference electrode (RE). The electrochemical method was applied using an AUTOLAB PGSTAT 12 (Eco-Chemie) controlled by the software GPES v4.9. After the ED was performed, the protocol was transferred to a miniaturized setup composed of SPCE from Dropsens (DRP-110), and the portable potentiostat SensitSmart from Palmsens, controlled by the PSTrace 5.9 on a Windows PC.

2.3. FESEM characterization

High-Resolution Field Emission Scanning Electron Microscopy (HR FESEM, Zeiss Auriga Microscopy, Jena, Germany) was used to scan the SPCE surface. The samples were prepared according to the protocol outlined in the following section. Size-distribution curves were obtained using ImageJ analysis software, version 1.37.

2.4. Electrode modification

Prior to use, the unmodified SPCE was thoroughly rinsed with Milli-Q water and subsequently dried under a pure nitrogen flow twice, in order to eliminate any impurities that may have been adsorbed onto the surface. Gold ED was carried out in a 10 mM $[AuCl_4]^-$ solution with 0.1 M $NaNO_3$ as electrolyte, previously deaerated with N_2 for 20 mins by applying a potential window ranging from 1.1 to 0.1 V vs $Ag/AgCl_{sat}$ [46], at a scan rate of 50 mV/s. Specifically, different concentrations of $[AuCl_4]^-$ precursor were tested (from 0.25 to 15 mM), as well as a different number of CV cycles (from 5 to 25). The electrodes were then electrochemically activated in 0.5 M H_2SO_4 at 50 mV/s, and washed in water several times until the pH turned neutral [45]. Next, the electrodes were incubated in a 2 mM MPA solution for different times, in the dark, to avoid thiolate formation by UV radiation. Any excess potentially physisorbed on the surface was removed by washing the surface with ethanol. As soon as the surface was dry, the electrodes were left to react for 15 mins with a freshly prepared solution of 0.1 mM EDC and 0.5 mM NHS, to activate the MPA carboxylic groups.

The surface was then rinsed with MES buffer pH 5.4 and left to dry at room temperature for about 30 mins. Afterwards, the electrodes were incubated in 15 μL of 10 μg/mL Ab_{NGAL} for 30 mins to allow the nucleophile attack of Ab's amino residues. Next, the electrodes were rinsed with 10 mM MES buffer, pH 5.4 and left to stabilize overnight at 4 °C with covered by 100 μL of 10 mM PBS buffer 7.4. This step was carried out in a custom-built humidity chamber to ensure a wet envoironment that prevents protein denaturation. Prior to antigen incubation, the surface was blocked with 0.1 mg/mL BSA for 20 mins to deactivate any active sites potentially exposed by the antibody molecules, thus avoiding nonspecific interactions and enhancing antigen-binding selectivity. The surface was then gently rinsed with 10 mM PBS (pH 7.4) and incubated with 15 μL of the prepared NGAL solution. Finally, the surface was gently rinsed with PBS, and incubated with 15 μL of a given NGAL solution.

2.5. NGAL calibration with standards

The modified electrodes - Ab/MPA/AuNP/SPCE - were incubated with different concentrations of NGAL for 30 mins, and then rinsed with PBS, pH 7.4. Once the surface was dry the electrode was tested in a solution of 1.1 mM $[Fe(CN)_6]^{3-/4-}$, 0.1 M KCl, using the Differential Pulse Voltammetry (DPV) technique.

2.6. Interferent species

Selectivity tests were performed by incubating the Ab/MPA/AuNP/SPCE modified electrodes in 15 μL of NGAL standard solutions containing several substances normally present in high concentration in serum samples, namely: 1.0 mM glutamic acid, 4 mM glycine, 0.1 mM ascorbic acid, and 4 mM urea.

2.7. Analysis of real samples

The sensor's accuracy was validated by testing the modified electrodes in real matrixes. To this aim, fresh urine samples were centrifuged at 5000 rpm for 10 mins. Spiked urine samples were prepared by adding a known amount of NGAL to the collected supernatant. The signal was correlated to the NGAL concentration obtained with the calibration curve, and the Recovery values were calculated with eq. (1)

$$Recovery = 100x(C_{obs} - C_{end})/C_{spiked} \quad (1)$$

3. Results and discussion

3.1. Overview of the electrodeposition process by cyclic voltammetry (AuNPs/SPCE)

Aiming to optimize the AuNPs ED process, different concentrations of $[AuCl_4]^-$ precursor were initially tested, as well as the total number of CVs. According to the literature, the following overall deposition reaction takes place (1):

$$[AuCl_4]^- + 3e - \rightarrow Au + 4Cl^- \; E^0 = 1.00\ V/SHE \quad (1a)$$

To prevent the formation of bigger aggregates often reported when using KCl (results not shown), $NaNO_3$ was preferred as the supporting electrolyte [26]. In such electrolytes, [47] the detailed mechanism of reaction (1) consists of an initial chemical reaction followed by two charge transfer steps [27,30,47–49]:

$$[AuCl_4]^- \Leftrightarrow [AuCl_2]^+ + 2\ Cl^- \quad (2)$$

$$[AuCl_2]^+ + 2e- \Rightarrow [AuCl_2]^- \quad (3)$$

$$[AuCl_2]^- + e^- \Rightarrow Au + 2\ Cl^- \quad (4)$$

In Fig. 1A, the first scan reveals a considerable overpotential for the metal deposition with respect to the following scans, suggesting that the stripping process is not fully completed. This indicates once the first gold particles are formed on the electrode surface, the subsequent growth occurs primarily at these residual gold sites rather than on the graphite [50]. Moving to the second scan, the peak potential of the reduction of Au^{3+} to Au^0 shifts from 0.35 (1st scan) to 0.55 V vs $Ag|AgCl_{sat.}$ (ΔV_{1st_2nd} =200 mV). During the backward scan, a current crossover can be detected at 0.230 V vs $Ag|AgCl_{sat.}$, beyond which the backward cathodic current is higher than the forward one [51]. These potential shifts are consistent with the fact that AuNPs deposition on a gold layer is a more thermodynamically favorable process than AuNPs nucleation on bare graphite [26]. A higher overpotential and a larger shift between the first and the second scan has been reported in the case of gold nucleation on GC electrodes with peak potential shifts around ΔV_{1st_2nd} =400 mV. These findings support the hypothesis that SPCEs provide a more reactive surface for gold nucleation due to their greater surface irregularity compared to those of GC [52]. As reported in Fig. 1B, the shift progressively moves towards more positive potentials until the end of the process.

To provide a clearer understanding of the changes occurring at the

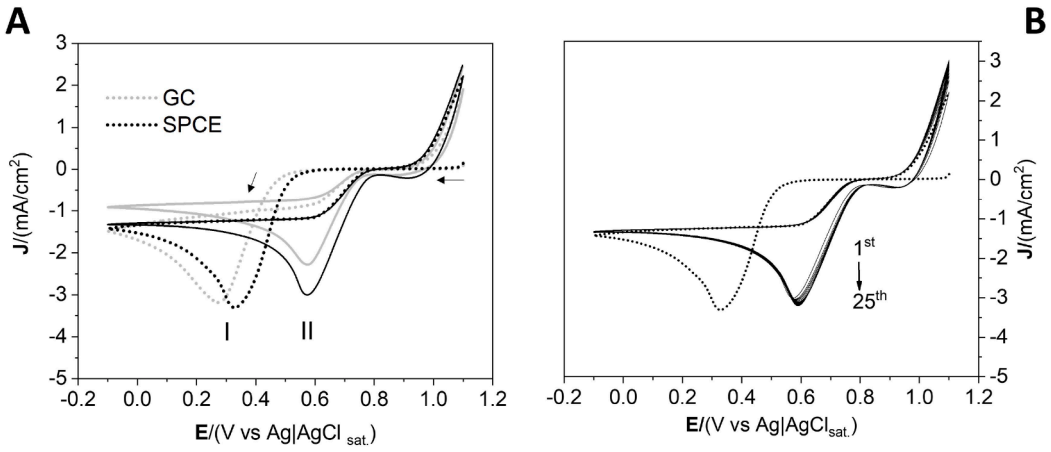

Fig. 1. (A) Potential shift of the Au^{3+} reduction peak among the 1st (dotted line) and 2nd (solid) CVs on SPCE (black lines) and GC (gray lines) surfaces. **(B)** Sequential CVs performed between 1.1 and −0.1 V (vs $Ag/AgCl_{sat}$) in a 10 mM $[AuCl_4]^-$ deposition bath [51]. The CVs were performed in a N_2 saturated solution at 50 mV/s, (E_{step} = 0.002 V).

electrode surface with increasing cycles, SEM was performed along the entire process after 2, 5, 15, 25, and 30 scans. As shown in Fig. 2, a more pronounced gold nucleation is clearly observed in the presence of graphite irregularities when progressing from the 2nd to the 5th scan. This process is accompanied by a slight increase in the average particles diameter and in particular those of the smaller nuclei, resulting in a more uniform particles' distribution.

Gold continues to cover the remaining uncovered graphite sites until the end of the 25th scan, at which the surface appears fully coated with particles. By the 30th scan, the particles begin to grow perpendicularly to the electrode surface, forming multiple layers with empty spaces running through. Based on these observations, a 25-scan procedure was implemented to achieve a uniform monolayer of gold particles across the electrode surface.

3.2. Gold concentration influence on surface morphology

SEM measurements, presented in Fig. 3, illustrate the surface morphologies obtained using various concentrations of gold precursor. In agreement with previous studies, higher concentrations of $[AuCl_4]^-$ induce a transition in the nucleation process from a progressive to an instantaneous mode, thereby enhancing the efficiency of ED and significantly affecting the resulting particle diameters [53]. Specifically, precursor concentrations of 0.25 mM, 2.5 mM, 5 mM, and 10 mM result in nanoparticles of 25 nm, 50 nm, 150 nm, and 300 nm, respectively. While higher concentrations lead to a broader particle size distribution, the deposition bath with 2.5 mM $[AuCl_4]^-$ exhibits an unusual narrow particle size distribution. Moreover, to expand the understanding of the surface morphology changes, SEM were reported over the following scans at each of the precursor concentrations (**Fig. S1a-d**).

Considering the CVs of a given gold precursor concentration, a shift towards more negative potentials can be observed in the peak potential (Fig. 4A). Two factors can be related to this phenomenon: i) a slower precursor diffusion [54] towards the electrode surface attributable to the decrease in concentration gradient between bulk and electrode surface when the $[AuCl_4]^-$ concentration becomes too high; ii) a less effective catalysis of the following nucleation cycles, due to the bigger AuNPs sizes obtained under higher concentrations [55]. To analyze the different platforms one cannot compare the electroactive areas (A_{el}) and real surface areas (A_{real}) because in the first case, the high CV's capacitive current impeded a rigorous calculation; whereas in the second case, the overall electrode material is not considered a traditional polycrystalline gold electrode, which is the main condition when the one-to-one adsorption of oxygen method is applied [56]. Therefore, a comparative analysis was done by assessing the integrated areas of the AuO reduction peaks (A_{AuO}) obtained with CV at 100 mV/s in 0.5 M

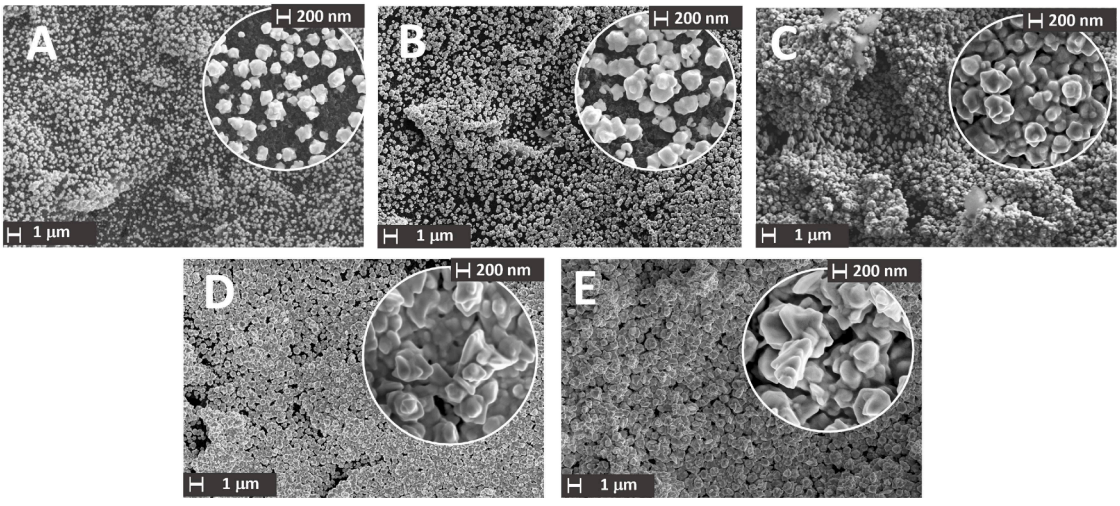

Fig. 2. SEM experiments showing the evolution of the SPCE surface throughout the entire electrodeposition process in a 10 mM $[AuCl_4]^-$, 0.1 M $NaNO_3$ solution after **(A)** 2 **(B)** 5, **(C)** 15, **(D)** 25 and **(E)** 30 scans. SEM were collected at two different magnifications (10 K x with a 50 K x inset).

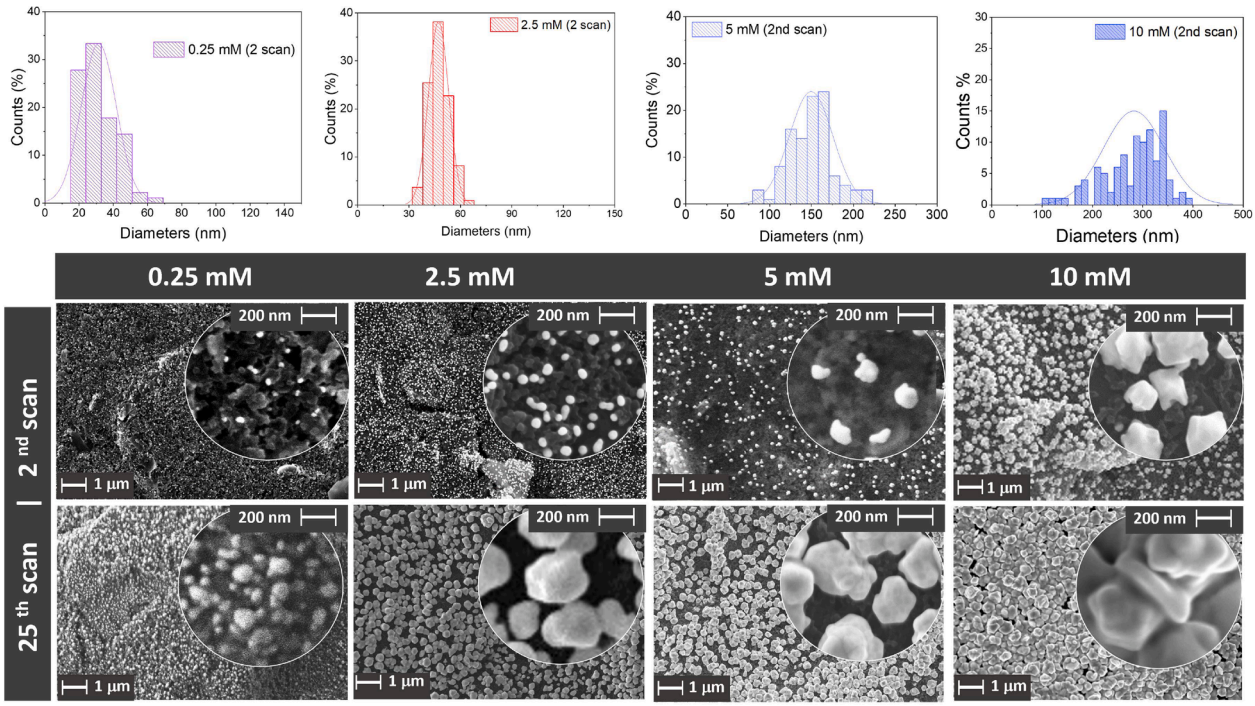

Fig. 3. SEM of electrodeposited AuNPs on SPCE electrode after 2 and 25 scans prepared using $[AuCl_4]^-$ of 0.25 mM, 2.5 mM, 5 mM and 10 mM at two different magnifications. Size-distribution curves were placed above each modification. The profiles were obtained by analysing each SEM with ImageJ software.

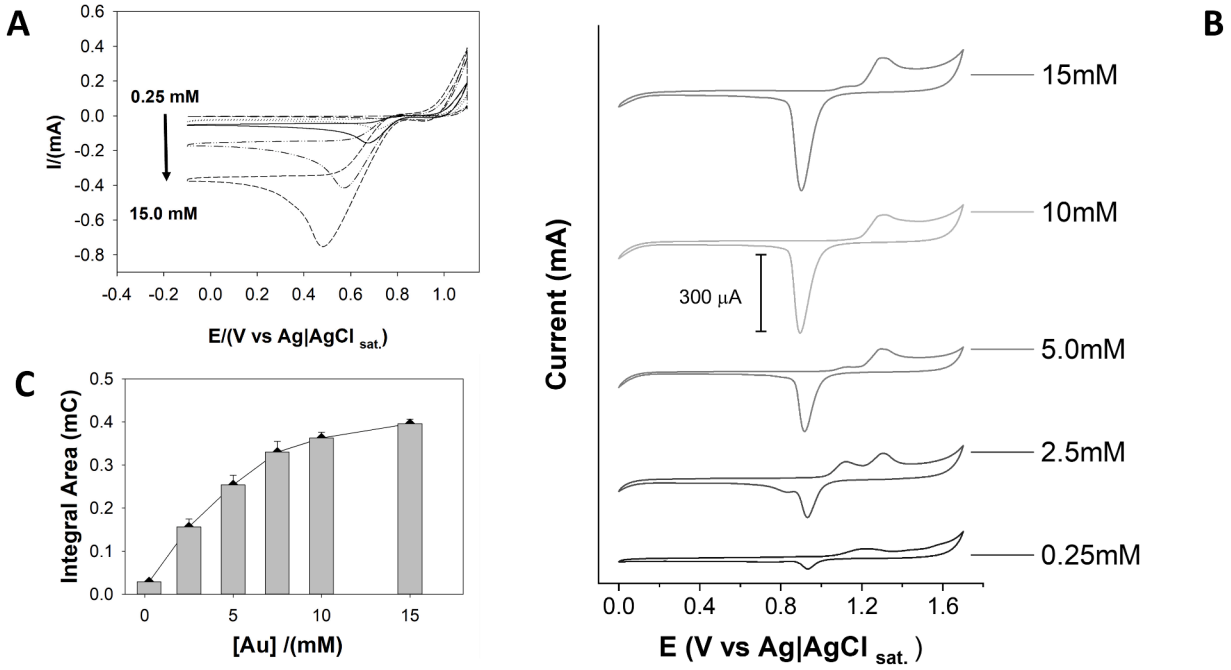

Fig. 4. **(A)** Comparison among the 25th scan of ED processes obtained with different precursor concentrations (0.25; 2.5; 5; 10 and 15 mM) using 0.1 M NaNO3 as supporting electrolyte. The CVs were performed by sweeping the voltammetry between 1.1 to −0.1 V vs Ag|AgCl $_{sat.}$ at 50 mV/s with an E_{step}= 0.002 V. **(B)** CVs performed at 100 mV/s in a freshly preparet 0.5 M H_2SO_4 solution after modifying the SPCE with different $[AuCl_4]^-$. (**C**) Integration peak at 0.9 V vs Ag|$AgCl_{sat.}$ behavior exhibiting saturation between 10 and 15 mM.

H_2SO_4, for each precursor concentration (Fig. 4B, C). Above 10 mM, the A_{AuO} did not increase much ($A_{AuO15mM}/A_{AuO10mM}$=1.09), representing the starting point of the plateaux, i.e., the maximum reachable coverage. The 2.5 and 10 mM $[AuCl_4]^-$ concentrations were chosen as references of the lower (0–5 mM) and higher concentration (5–15 mM) ranges, respectively, to evaluate their performance in the subsequent construction of label-free sensing platforms.

Interestingly, the 2.5 mM platform exhibited increased reactivity when exposed to a ferrocyanide redox probe. The obtained voltammogram is compatible with the production of prussian blue (PB) on Au [110] crystal facet [57], which is responsible for effectively catalysing the PB formation, decreasing the energy required for the process and

providing unusual sharp peaks in respect those obtained in the case of polycrystalline gold substrates (**Figure S2**). Notably, the etching voltammogram obtained for the 2.5 mM precursor concentration, exhibits several characteristics that aligns to those reported in the literature for the Au[110] crystal facet in H_2SO_4, including [58–60]: i) the presence of two closely spaced oxidation peaks at $E > 1.05$ V, specifically at 1.1 V and 1.3 V; ii) the occurrence of a second reduction peak at 0.80 V, in addition to the classic gold reduction peak at 0.90 V, which is consistently absent in the etching of Au[111] and Au[100] single-crystal electrodes in H_2SO_4 solutions [61–65]. These results, together with the observed PB voltammogram, support the hypothesis that this modification promotes the preferential formation of the Au[110] facet.

Such reactive modifications could be an advantage in the case of enzymes are not auspicious for the fabrication of immunosensors because they interfere with the probe solution. Therefore, the 10 mM precursor concentration was chosen for the following steps, which also represents a good compromise to achieve a high reproducibility (Fig. 4C) with the minimum amount of the gold precursor.

3.3. Surface comparison with commercial gold SPE

The surface morphology and composition of commercial polycrystalline gold screen-printed electrodes (SPEs) and electrodeposited gold screen-printed carbon electrodes were characterized using SEM and EDX spectroscopy. Specifically, Fig. 5A illustrates the presence of a macroscopic polycrystalline gold layer on the surface of the commercial gold SPEs. Although these substrates are less effective than AuNPs in amplifying the electrochemical signal, they are particularly well-suited for thiol functionalization, which is critical for biosensing applications. However, several regions on the SPE surface exhibit incomplete gold coverage, where the underlying substrate is directly exposed. These areas—highlighted in red—are prominent on the electrode surface and indicate the presence of aluminum (Al) and silicon (Si), which reduces the homogeneity of the surface, critical for preventing nonspecific absorption in complex matrices.

This drawback is not observed in the case of our platform (Fig. 5D-F), where the surface is completely covered with gold. Additionally, two key findings from the EDX analysis are remarkable: (i) a more extensive nucleation and subsequent coalescence of nanoparticles occurs in regions where the carbon signal is more intense, such as at surface irregularities (Fig. 5E); and (ii) The SPCE surface promotes gold nucleation more efficiently than GC. These findings are consistent with the potential shifts discussed in *Section 3.1.*, highlighting that the electrodeposition process is particularly effective for SPCEs, resulting in a stable and reproducible surface for immunosensing applications.

3.4. SAM optimization and Ab immobilization on AuNPs/SPCE

After having optimised the modification procedure, the gold-covered electrode was incubated in a solution of 2 mM MPA and tested over time through EIS measurements using $[Fe(CN)_6]^{3-/4-}$ as a redox probe, to follow the SAM formation on the SPCE/AuNPs. The SAM blocking effect of the resulting MPA/AuNP/SPCE on the $[Fe(CN)_6]^{3-/4-}$electrochemistry increased progressively over the first 12 h of MPA incubation but stabilized during the next 12 h (**Fig. S3A**). By comparing the R_{ct} values obtained from the Nyquist plot by fitting the circuit (**Fig. S3B**), we observed that between the timeframe 12 - 24 h, the electrode resistance did not increase much and so did the thiol coverage of the gold electrode. For this reason, a 12 h incubation time was chosen as the optimal condition for the complete SAM formation. After the SAM formation had been optimized, the electrodes were treated with EDC/NHS and then with the Ab_{NGAL}. The Ab immobilization was then assessed by EIS spectroscopy (**Fig. S4**).

3.5. Sensor calibration and analytical performances

Sensor calibration was performed by treating the surface with different concentrations of NGAL. The electrodes were tested using DPV in a 1.1 mM $[Fe(CN)_6]^{3-/4-,}$ 100 mM KCl solution producing the curves shown in Fig. 6A. The ΔI obtained were plotted as function of the NGAL concentration to construct a calibration curve (Fig. 6B) until saturation occurred (**Fig. S5**). According to the literature, the obtained linear range 0.10 – 50 μg/mL and the sensitivity of 21.58 μA mL/μg make it suitable for AKI diagnosis. Moreover, the reproducibility was assessed by testing five independent electrodes; the graph shown in Fig. 6C reports the peak intensity obtained for each immunosensor replicate. The RSD calculated was around 4.5%, demonstrating the consistency of electrode preparation (Scheme 1).

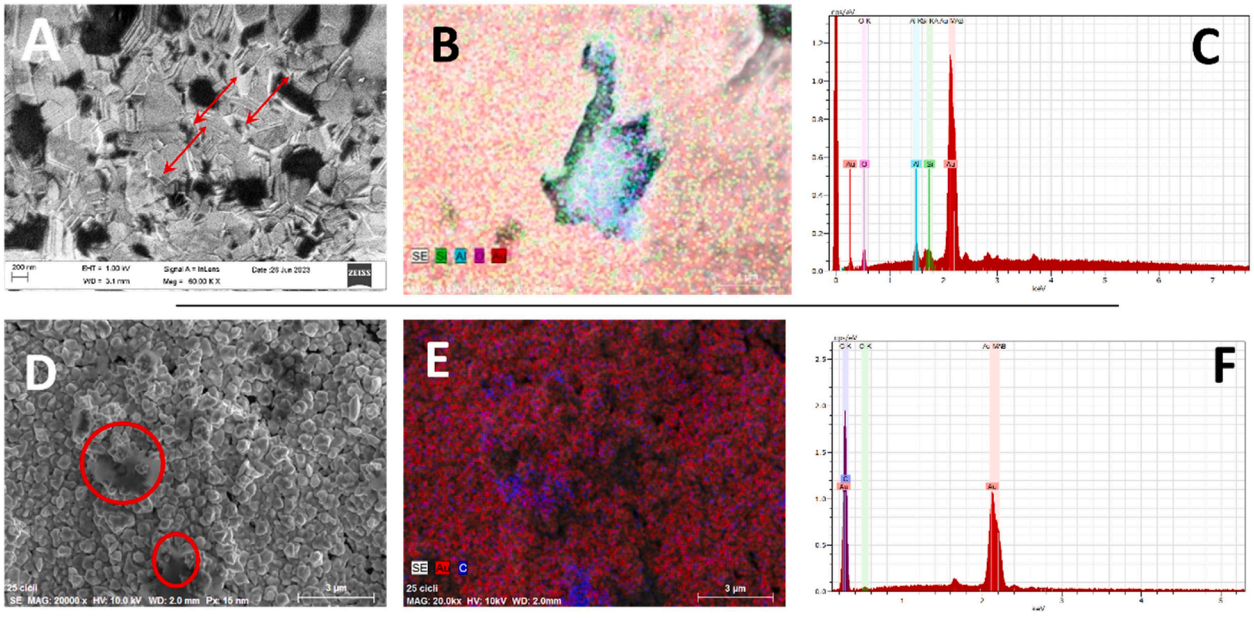

Fig. 5. Comparison of the SEM and EDX spectra obtained for a commercial gold SPE (**A, B, C**) and our gold-electrodeposited SPCE (**D, E, F**). The red arrows identify the areas where the commercial electrode exhibits residual contamination with aluminum and silicon, which are absent in our platform. The red circles indicate regions of more intense nucleation, particularly at surface irregularities.

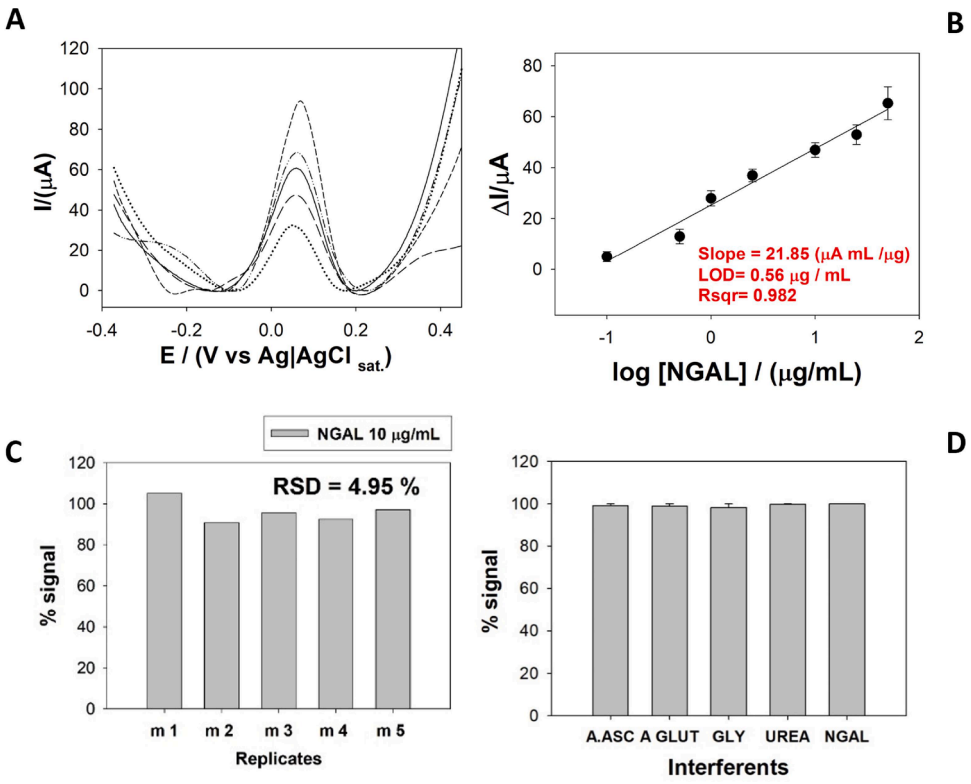

Fig. 6. **(A)** DPV peaks and concentration profiles obtained by using a scan rate of 0.1 V/s with an E_{step} of 0.002 V in a probe solution containing 1.1 mM $[Fe(CN)_6]^{3-/4-}$, 0.1 M KCl. **(B)** calibration curve obtained after the incubation of several NGAL standards prepared in PBS buffer 10 mM, pH 7.4, on the immunosensor platform **(C)** Replicates acquired following the incubation of 10 μg/mL NGAL on the SPCE/AuNPs/MPA/Ab/BSA modified electrode. **(D)** DPV peaks obtained after NGAL interaction in the presence of interfering species, namely: 1.0 mM glutamic acid, 4 mM glycine, 0.1 mM ascorbic acid, and 4 mM urea.

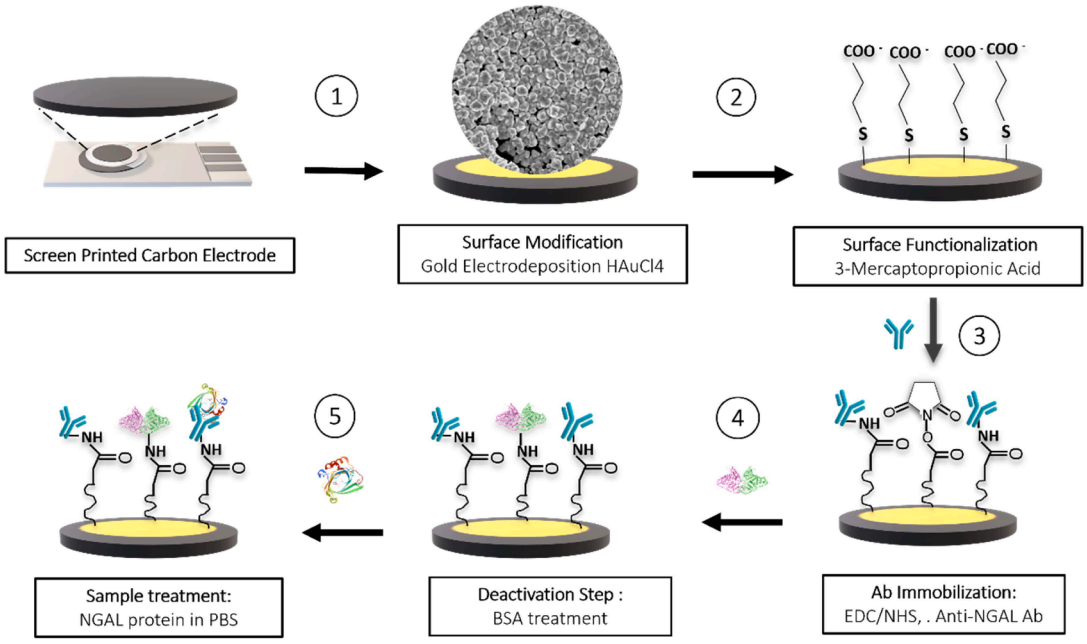

Scheme 1. Scheme of the sensor assembly representing the each step involved in the sensor development, including: 1) Electrochemical deposition of gold. 2) Surface modification with a thiol layer (MPA). 3) Activation of the carboxylic mojeties through EDC/NHS cross-linking. 4) Ab_{NGAL} immobilization 5) Surface blocking with BSA. 6) Antigen (NGAL) interaction.

Furthermore, to better understand the sensor's true capability of working in complex environments, its performance was evaluated in the presence of several common interfering species exceeding 10^6 -fold the antigen concentration. The no significant signal variation demonstrates a significant lack of Ag-Ab complex disruption and confirms the great capability of the Ab/MPA/AuNP/SPCE immunosensor to work in real matrices. Moreover, an excellent reproducibility was again obtained (< 2%). Therefore, as a proof of concept, the sensor was tested in real urine

samples through recovery tests. The values ranges from 91 to 111 suggesting its potential uses in pretreated samples (Table 1).

Compared to other works in the literature, our sensor can provide a rapid and miniaturized platform with the required effectiveness for the diagnostic range of AKI while optimizing the surface modification, simplifying the fabrication procedure significantly, and reducing its costs. Unlike other label-free immunosensors [43,44], it does not require any additional or specific equipment, organic solvents, or gold-reducing agents. In regard to the labelled ones, it minimizes the response time and avoids the use of additional reagents, such as the highly costly labelled antibodies. An interesting observation can be pointed out by comparing the linear ranges of the two platforms. Despite the lower LOD achieved by the sandwich immunoassay approach used by Neves, [35] our sensor extended the linear range of the AuNPs/SPCE to the range 0.10 – 50 μg/mL. This can be due to a greater number of antibody binding sites available for the antigen interaction. This hypothesis is consistent with the presence of a greater amount of gold hosting the captured antibody with respect to the single, spaced-out nuclei described by Neves [41]. Also, the extensive optimization step allowed the sensor to maintain its effectiveness despite the lower amount of antibody used when compared to other platforms such as the 3D-graphene-based immunosensor [66], which uses antibody quantities in the range of 0.3 – 10 mg/mL. The Yukrid's work [42], in particular, shows comparable analytical parameters by immobilizing an antibody amount over 30 times higher. Therefore, our gold-electrodeposited platform succeeds in optimizing the antibody quantity while improving surface modification and providing a reproducible, impurity-free surface. This establishes our electrochemical immunosensor not only as a fast and miniaturized tool for the detection of NGAL protein but also as a versatile approach that can be easily adapted to other immunosensor applications.

4. Conclusions

Herein, we have discussed regarding the optimization of gold ED process through CV technique in order to develop a stable and reproducible surface for immunosensing applications. Several procedures were set up by using different gold precursor concentrations in the same potential range and a different number of scans. Specifically, the effect of the $[AuCl_4]^-$ concentration was evaluated between almost two orders of magnitude (0.25 – 10 mM). Moreover, SEM experiments were performed to carefully investigate the surface morphology and to assess the nanoparticles' size and shape along the concentration interval. Accordingly, NPs ranging from 25, 50, 150, and 300 nm diameters were deposited by employing 0.25, 2.5, 5.0, and 10 mM precursor concentrations respectively. The modification obtained with the 10 mM gold precursor provided the most stable platform, exhibiting a reproducible integral area of AuO reduction peak, good stability in the probe solution, and a total gold coverage of SPCE surface. Furthermore, for comparison purposes, the surface morphology of a commercial gold electrode was investigated by EDX analysis, and the composition was compared to that of our platform to conclude the substantial absence of contaminants in the latter one. The optimized procedure was then employed in the development of an immunosensor for NGAL detection, by modifying the gold electrodeposited platform with a self-assembled monolayer of MPA and subsequently crosslinking the exposed carboxylic moieties with the NGAL antibody through EDC/NHS coupling. The electrodes were tested to detect the NGAL protein and to assess its ability to predict acute kidney injury. The substantial absence of interference with common urine molecules and the ability to detect the NGAL in spiked urine samples suggest the excellent capability of the sensor to work in real matrices. Compared to previous works, our sensor provides a quick and miniaturizable tool for NGAL detection, simplifying the fabrication process and optimizing the amount of antibody on the surface.

Table 1
Recovery values and RSD reported after testing NGAL spiked urine samples. Each sample has been tested in triplicate by performing a DPV measurement in a 1.1 mM $[Fe(CN)_6]^{3-/4-}$, 0.1 M KCl at 0.1 V/s, Estep= 0.002 V.

NGAL Concentration in Spiked Urine Samples (μg/mL)	Recovery (%)	E_a %	RSD (%)
20	91.10	−0.098	5.95
50	110.5	0.095	4.76
2	93.00	0.007	3.13

CRediT authorship contribution statement

Francesca Polli: Writing – original draft, Investigation, Data curation, Conceptualization. **Rosaceleste Zumpano:** Writing – review & editing, Investigation. **Gianluca Zanellato:** Investigation, Data curation. **Sofia de Azeredo Pereira:** Resources, Conceptualization. **Alessandro Fantoni:** Funding acquisition. **Franco Mazzei:** Writing – review & editing. **M . Gabriela Almeida:** Writing – review & editing, Supervision, Project administration, Investigation, Conceptualization.

Declaration of competing interest

The authors declare that they have no known competing financial interests or personal relationships that could have appeared to influence the work reported in this paper.

Acknowledgments

This work is financed by national funds through the FCT - Foundation for Science and Technology, I.P., under the projects UIDB/04585/2020 (Research Center - CiiEM), UIDP/04378/2020 and UIDB/04378/2020 (Research Unit on Applied Molecular Biosciences - UCIBIO), and LA/P/0140/2020 (Associate Laboratory Institute for Health and Bioeconomy - i4HB) and UIDB/00066/2020/UIDP/00066/2020 (Center of Technology and Systems - CTS).

Supplementary materials

Supplementary material associated with this article can be found, in the online version, at doi:10.1016/j.electacta.2025.145787.

Data availability

Data will be made available on request.

References

[1] G. Siciliano, A. Alsadig, M.S. Chiriacò, A. Turco, A. Foscarini, F. Ferrara, G. Gigli, E. Primiceri, Beyond traditional biosensors: recent advances in gold nanoparticles modified electrodes for biosensing applications, Talanta 268 (2024), https://doi.org/10.1016/j.talanta.2023.125280.
[2] P. Bollella, Biosensors — Recent Advances and Future Challenges, Sensors 20 (22) (2020) 6645. https://doi.org/10.3390/s20226645.
[3] R.C. Salvarezza, P. Carro, The electrochemical stability of thiols on gold surfaces, J. Electroanal. Chem. 819 (2018) 234–239, https://doi.org/10.1016/j.jelechem.2017.10.046.
[4] S. Ge, J. Zhao, G. Ma, Thiol stabilized extremely small gold cluster complexes with high photoluminescence, Inorg. Chem. Commun. 109 (2019), https://doi.org/10.1016/j.inoche.2019.107556.
[5] E. Ferrari, Gold Nanoparticle-Based Plasmonic Biosensors, Biosensors. (Basel) (2023) 13, https://doi.org/10.3390/bios13030411.
[6] M.A. Farzin, H. Abdoos, R. Saber, AuNP-based biosensors for the diagnosis of pathogenic human coronaviruses: COVID-19 pandemic developments, Anal. Bioanal. Chem. (2022), https://doi.org/10.1007/s00216-022-04193-2.
[7] M.A. Sadique, S. Yadav, P. Ranjan, R. Khan, F. Khan, A. Kumar, D. Biswas, Highly sensitive electrochemical immunosensor platforms for dual detection of SARS-CoV-2 Antigen and Antibody based on Gold Nanoparticle Functionalized Graphene Oxide Nanocomposites, ACS. Appl. Bio Mater. 5 (2022) 2421–2430, https://doi.org/10.1021/acsabm.2c00301.

[8] M. Asif, M. Ajmal, G. Ashraf, N. Muhammad, A. Aziz, T. Iftikhar, J. Wang, H. Liu, The role of biosensors in coronavirus disease-2019 outbreak, Curr. Opin. Electrochem. 23 (2020) 174–184, https://doi.org/10.1016/j.coelec.2020.08.011.

[9] F. Polli, F. Simonetti, L. Surace, M. Agostini, G. Favero, F. Mazzei, R. Zumpano, Nanoparticles in Electrochemical Immunosensors – A Concept and Perspective, ChemElectroChem. 11 (2024), https://doi.org/10.1002/celc.202300408.

[10] M.L. Yola, N. Atar, N. Özcan, A novel electrochemical lung cancer biomarker cytokeratin 19 fragment antigen 21-1 immunosensor based on Si3N4/MoS2incorporated MWCNTs and core-shell type magnetic nanoparticles, Nanoscale 13 (2021) 4660–4669, https://doi.org/10.1039/d1nr00244a.

[11] Ö.S. Bölükbaşi, B.B. Yola, C. Karaman, N. Atar, M.L. Yola, Electrochemical α-fetoprotein immunosensor based on Fe3O4NPs@covalent organic framework decorated gold nanoparticles and magnetic nanoparticles including SiO2@TiO2, Microchimica Acta 189 (2022), https://doi.org/10.1007/s00604-022-05344-z.

[12] B.B. Yola, C. Karaman, N. Özcan, N. Atar, İ. Polat, M.L. Yola, Electrochemical Tau Protein Immunosensor Based on MnS/GO/PANI and Magnetite-incorporated Gold Nanoparticles, Electroanalysis. 34 (2022) 1519–1528, https://doi.org/10.1002/elan.202200159.

[13] C. Karaman, Ö.S. Bölükbaşı, B.B. Yola, O. Karaman, N. Atar, M.L. Yola, Electrochemical neuron-specific enolase (NSE) immunosensor based on CoFe2O4@Ag nanocomposite and AuNPs@MoS2/rGO, Anal. Chim. Acta (2022) 1200, https://doi.org/10.1016/j.aca.2022.339609.

[14] O. Karaman, N. Özcan, C. Karaman, B.B. Yola, N. Atar, M.L. Yola, Electrochemical cardiac troponin I immunosensor based on nitrogen and boron-doped graphene quantum dots electrode platform and Ce-doped SnO2/SnS2 signal amplification, Mater. Today Chem. 23 (2022), https://doi.org/10.1016/j.mtchem.2021.100666.

[15] M. Lütfi Yola, N. Atar, Novel voltammetric tumor necrosis factor-alpha (TNF-α) immunosensor based on gold nanoparticles involved in thiol-functionalized multi-walled carbon nanotubes and bimetallic Ni/Cu-MOFs, (n.d.). https://doi.org/10.1007/s00216-021-03203-z/Published.

[16] V.R. Samuel, K.J. Rao, A review on label free biosensors, Biosens. Bioelectron. X. (2022) 11, https://doi.org/10.1016/j.biosx.2022.100216.

[17] R. Cancelliere, E. Paialunga, A. Grattagliano, L. Micheli, Label-free electrochemical immunosensors: a practical guide, TrAC - Trends Anal. Chem. 180 (2024), https://doi.org/10.1016/j.trac.2024.117949.

[18] R. Shegokar, M. Nakach, Chapter 4 - Large-scale manufacturing of nanoparticles—an industrial outlook, in: R. Shegokar (Ed.), Drug Delivery Aspects, Elsevier, 2020, pp. 57–77, https://doi.org/10.1016/B978-0-12-821222-6.00004-X.

[19] M. Zamani, C.M. Klapperich, A.L. Furst, Recent advances in gold electrode fabrication for low-resource setting biosensing, Lab. Chip. 23 (2023) 1410–1419, https://doi.org/10.1039/d2lc00552b.

[20] E. Bernalte, C. Marín-Sánchez, E. Pinilla-Gil, C.M.A. Brett, Characterisation of screen-printed gold and gold nanoparticle-modified carbon sensors by electrochemical impedance spectroscopy, J. Electroanal. Chem. 709 (2013) 70–76, https://doi.org/10.1016/j.jelechem.2013.09.007.

[21] W. Wang, A.A. Ignatius, S.V. Thakkar, Impact of residual impurities and contaminants on protein stability, J. Pharm. Sci. 103 (2014) 1315–1330, https://doi.org/10.1002/jps.23931.

[22] A. Kaliyaraj Selva Kumar, Y. Zhang, D. Li, R.G. Compton, A mini-review: how reliable is the drop casting technique? Electrochem. commun. 121 (2020) 106867 https://doi.org/10.1016/j.elecom.2020.106867.

[23] C. Hou, Q. Luo, Y. He, H. Zhang, Potentiostatic electrodeposition of gold nanoparticles: variation of electrocatalytic activity toward four targets, J. Appl. Electrochem. 51 (2021) 1721–1730, https://doi.org/10.1007/s10800-021-01604-7.

[24] A.J. Ritz, O.M. Stuehr, D.N. Comer, R.A. Lazenby, Controlling Gold Morphology Using Electrodeposition for the Preparation of Electrochemical Aptamer-Based Sensors, ACS. Appl. Bio Mater. 7 (2024) 1925–1935, https://doi.org/10.1021/acsabm.3c01254.

[25] K. Zhang, J. Wei, H. Zhu, F. Ma, S. Wang, Electrodeposition of gold nanoparticle arrays on ITO glass as electrode with high electrocatalytic activity, Mater. Res. Bull. 48 (2013) 1338–1341, https://doi.org/10.1016/j.materresbull.2012.12.029.

[26] G. Gotti, K. Fajerwerg, D. Evrard, P. Gros, Electrodeposited gold nanoparticles on glassy carbon: correlation between nanoparticles characteristics and oxygen reduction kinetics in neutral media, Electrochim. Acta 128 (2014) 412–419, https://doi.org/10.1016/j.electacta.2013.10.172.

[27] Y. Tian, H. Liu, G. Zhao, T. Tatsuma, Shape-controlled electrodeposition of gold nanostructures, J. Phys. Chem. B 110 (2006) 23478–23481, https://doi.org/10.1021/jp065292q.

[28] P. Bollella, L. Gorton, R. Ludwig, R. Antiochia, A third generation glucose biosensor based on cellobiose dehydrogenase immobilized on a glassy carbon electrode decorated with electrodeposited gold nanoparticles: characterization and application in human saliva, Sensors (Switzerland) (2017) 17, https://doi.org/10.3390/s17081912.

[29] N.D. Zakaria, M.H. Omar, N.N. Ahmad Kamal, K. Abdul Razak, T. Sönmez, V. Balakrishnan, H.H. Hamzah, Effect of supporting background electrolytes on the nanostructure morphologies and electrochemical behaviors of electrodeposited gold nanoparticles on glassy carbon electrode surfaces, ACS. Omega 6 (2021) 24419–24431, https://doi.org/10.1021/acsomega.1c02670.

[30] M.H. Mohd Zaki, Y. Mohd, L.Y. Chin, Surface properties of nanostructured gold coatings electrodeposited at different potentials, Int. J. Electrochem. Sci. 15 (2020) 11401–11415, https://doi.org/10.20964/2020.11.41.

[31] M.C. Tanzi, S. Farè, G. Candiani, Organization, structure, and properties of materials, Found. Biomater. Eng. (2019) 3–103, https://doi.org/10.1016/B978-0-08-101034-1.00001-3.

[32] K.J. Stine, Biosensor applications of electrodeposited nanostructures, Appl. Sci. (Switzerland) (2019) 9, https://doi.org/10.3390/app9040797.

[33] Y. Jiang, X. Zhang, C. Shan, S. Hua, Q. Zhang, X. Bai, L. Dan, L. Niu, Functionalization of graphene with electrodeposited Prussian blue towards amperometric sensing application, Talanta 85 (2011) 76–81, https://doi.org/10.1016/j.talanta.2011.03.028.

[34] P. Devarajan, NGAL for the detection of acute kidney injury in the emergency room, Biomark. Med. 8 (2014) 217–219, https://doi.org/10.2217/bmm.13.149.

[35] P. Kannan, H.Y. Tiong, D.H. Kim, Highly sensitive electrochemical determination of neutrophil gelatinase-associated lipocalin for acute kidney injury, Biosens. Bioelectron. 31 (2012) 32–36, https://doi.org/10.1016/j.bios.2011.09.036.

[36] V. Au, J. Feit, J. Barasch, R.N. Sladen, G. Wagener, Urinary Neutrophil Gelatinase–Associated Lipocalin (NGAL) Distinguishes Sustained From Transient Acute Kidney Injury After General Surgery, Kidney Int. Rep. 1 (2016) 3–9, https://doi.org/10.1016/j.ekir.2016.04.003.

[37] W. Shang, Z. Wang, The Update of NGAL in Acute Kidney Injury, Curr. Protein Pept. Sci. 18 (2016), https://doi.org/10.2174/1389203717666160909125004.

[38] H. Boyacıoğlu, B.B. Yola, C. Karaman, O. Karaman, N. Atar, M.L. Yola, A novel electrochemical kidney injury molecule-1 (KIM-1) immunosensor based covalent organic frameworks-gold nanoparticles composite and porous NiCo2S4@CeO2 microspheres: the monitoring of acute kidney injury, Appl. Surf. Sci. 578 (2022), https://doi.org/10.1016/j.apsusc.2021.152093.

[39] Y. Hu, X.A. Yu, Y. Zhang, R. Zhang, X. Bai, M. Lu, J. Li, L. Gu, J.H. Liu, B.Y. Yu, J. Tian, Rapid and sensitive detection of NGAL for the prediction of acute kidney injury: via a polydopamine nanosphere/aptamer nanocomplex coupled with DNase I-assisted recycling amplification, Analyst 145 (2020) 3620–3625, https://doi.org/10.1039/d0an00474j.

[40] E. Derin, F. Inci, Advances in Biosensor Technologies for Acute Kidney Injury, ACS. Sens. 7 (2022) 358–385, https://doi.org/10.1021/acssensors.1c01781.

[41] M.M.P.S. Neves, H.P.A. Nouws, A. Santos-Silva, C. Delerue-Matos, Neutrophil gelatinase-associated lipocalin detection using a sensitive electrochemical immunosensing approach, Sens. Actuators. B Chem. 304 (2020), https://doi.org/10.1016/j.snb.2019.127285.

[42] J. Yukird, T. Wongtangprasert, R. Rangkupan, O. Chailapakul, T. Pisitkun, N. Rodthongkum, Label-free immunosensor based on graphene/polyaniline nanocomposite for neutrophil gelatinase-associated lipocalin detection, Biosens. Bioelectron. 87 (2017) 249–255, https://doi.org/10.1016/j.bios.2016.08.062.

[43] K. Phonklam, W. Sriwimol, W. Thuptimdang, T. Phairatana, Disposable label-free electrochemical immunosensor based on gold nanoparticles-Prussian blue for neutrophil gelatinase-associated lipocalin detection in urine samples, Talanta 274 (2024), https://doi.org/10.1016/j.talanta.2024.125960.

[44] W.J. Wang, M.C. Chou, Y.J. Lee, W.L. Hsu, G.J. Wang, A simple electrochemical immunosensor based on a gold nanoparticle monolayer electrode for neutrophil gelatinase-associated lipocalin detection, Talanta 246 (2022), https://doi.org/10.1016/j.talanta.2022.123530.

[45] S.S. Kumar, J. Joseph, K.L. Phani, Novel method for deposition of gold-prussian blue nanocomposite films induced by electrochemically formed gold nanoparticles: characterization and application to electrocatalysis, Chemistry of Materials 19 (2007) 4722–4730, https://doi.org/10.1021/cm0711820.

[46] P. Bollella, L. Gorton, R. Ludwig, R. Antiochia, A Third Generation Glucose Biosensor Based on Cellobiose Dehydrogenase Immobilized on a Glassy Carbon Electrode Decorated with Electrodeposited Gold Nanoparticles: characterization and Application in Human Saliva, Sensors. (Basel) (2017) 17, https://doi.org/10.3390/s17081912.

[47] L. Komsiyska, G. Staikov, Electrocrystallization of Au nanoparticles on glassy carbon from HClO4 solution containing [AuCl4]-, Electrochim. Acta 54 (2008) 168–172, https://doi.org/10.1016/j.electacta.2008.08.013.

[48] O.I. Kuntyi, L.V. Sus, S.A. Kornii, E.V. Okhremchuk, Electrodeposition of Gold Nanoparticles in Dimethylformamide Solutions of H[AuCl4], Materials Science 51 (2016) 885–889, https://doi.org/10.1007/s11003-016-9917-1.

[49] J.C. Varia, S.S. Martinez, S. Velasquez-Orta, S. Bull, Microbiological influence of metal ion electrodeposition: studies using graphite electrodes, [AuCl4]− and Shewanella putrefaciens, Electrochim. Acta 115 (2014) 344–351, https://doi.org/10.1016/J.ELECTACTA.2013.10.166.

[50] S. Sobri, S. Roy, Gold Electrocrystallization from a Spent Thiosulfate-Sulfite Electrolyte, J. Electrochem. Soc. 152 (2005) C593, https://doi.org/10.1149/1.1979207.

[51] T. Hezard, K. Fajerwerg, D. Evrard, V. Collire, P. Behra, P. Gros, Gold nanoparticles electrodeposited on glassy carbon using cyclic voltammetry: application to Hg(II) trace analysis, Journal of Electroanalytical Chemistry 664 (2012) 46–52, https://doi.org/10.1016/j.jelechem.2011.10.014.

[52] J.D. Benck, B.A. Pinaud, Y. Gorlin, T.F. Jaramillo, Substrate selection for fundamental studies of electrocatalysts and photoelectrodes: inert potential windows in acidic, neutral, and basic electrolyte, PLoS. One 9 (2014), https://doi.org/10.1371/journal.pone.0107942.

[53] E. Sheridan, J. Hjelm, R.J. Forster, Electrodeposition of gold nanoparticles on fluorine-doped tin oxide: control of particle density and size distribution, Journal of Electroanalytical Chemistry 608 (2007) 1–7, https://doi.org/10.1016/j.jelechem.2006.11.015.

[54] G.J. Hills, D.J. Schiffrin, J. Thompson, Electrochemical nucleation from molten salts-I. Diffusion controlled electrodeposition of silver from alkali molten nitrates, Electrochim. Acta 19 (1974) 657–670, https://doi.org/10.1016/0013-4686(74)80008-3.

[55] X. Zhou, W. Xu, G. Liu, D. Panda, P. Chen, Size-dependent catalytic activity and dynamics of gold nanoparticles at the single-molecule level, J. Am. Chem. Soc. 132 (2010) 138–146, https://doi.org/10.1021/ja904307n.

[56] R. Zumpano, M. Manghisi, F. Polli, C. D'Agostino, F. Ietto, G. Favero, F. Mazzei, Label-free magnetic nanoparticles-based electrochemical immunosensor for atrazine detection, Anal. Bioanal. Chem. 414 (2022) 2055–2064.
[57] S. Nakanishi, G. Lu, H.M. Kothari, E.W. Bohannan, J.A. Switzer, Epitaxial Electrodeposition of Prussian Blue Thin Films on Single-Crystal Au(110), J. Am. Chem. Soc. 125 (2003) 14998–14999, https://doi.org/10.1021/ja0381151.
[58] K. Yoshida, A. Kuzume, P. Broekmann, I.V. Pobelov, T. Wandlowski, Reconstruction and electrochemical oxidation of Au(110) surface in 0.1 M H_2SO_4, Electrochim. Acta 139 (2014) 281–288, https://doi.org/10.1016/j.electacta.2014.06.162.
[59] A. Hamelin, Cyclic voltammetry at gold single-crystal surfaces. Part 1, Behaviour at low-index faces (1996).
[60] L.A. Kibler, Preparation and Characterization of Noble Metal Single Crystal Electrode Surfaces (2003). http://www.uni-ulm.de/echem.
[61] C. Jeyabharathi, P. Ahrens, U. Hasse, F. Scholz, Identification of low-index crystal planes of polycrystalline gold on the basis of electrochemical oxide layer formation, J. Solid State Electrochem. 20 (2016) 3025–3031, https://doi.org/10.1007/s10008-016-3228-1.
[62] C. Jeyabharathi, U. Hasse, P. Ahrens, F. Scholz, Oxygen electroreduction on polycrystalline gold electrodes and on gold nanoparticle-modified glassy carbon electrodes, J. Solid State Electrochem. 18 (2014) 3299–3306, https://doi.org/10.1007/s10008-014-2657-y.
[63] S. Yang, D.G.H. Hetterscheid, Redefinition of the active species and the mechanism of the oxygen evolution reaction on gold oxide, ACS. Catal. 10 (2020) 12582–12589, https://doi.org/10.1021/acscatal.0c03548.
[64] S. Liu, T. Ishimoto, M. Koyama, First-principles calculation of OH-/OH adsorption on gold nanoparticles, Int. J. Quantum. Chem. 115 (2015) 1597–1605, https://doi.org/10.1002/qua.24989.
[65] O. Diaz-Morales, F. Calle-Vallejo, C. De Munck, M.T.M. Koper, Electrochemical water splitting by gold: evidence for an oxide decomposition mechanism, Chem. Sci. 4 (2013) 2334–2343, https://doi.org/10.1039/c3sc50301a.
[66] P. Danvirutai, M. Ekpanyapong, A. Tuantranont, E. Bohez, S. Anutrakulchai, A. Wisitsoraat, C. Srichan, Ultra-sensitive and label-free neutrophil gelatinase-associated lipocalin electrochemical sensor using gold nanoparticles decorated 3D Graphene foam towards acute kidney injury detection, Sens. Biosensing. Res. 30 (2020), https://doi.org/10.1016/j.sbsr.2020.100380.